applied sciences

MDPI

Article

Research on Plastic Flow Characteristic Parameter Distribution of Shaped-Charge Jet: Theory, Experiment, and Simulation

Ping Song [1], Wenbin Li [2], Jianghai Liu [1], Qing Zhang [2] and Zhenxiong Wang [1,*]

[1] Research Institute of Chemical Defense, Academy of Military Science, Beijing 102205, China
[2] Ministerial Key Laboratory of ZNDY, Nanjing University of Science and Technology, Nanjing 210094, China
* Correspondence: wangzhenxiong70310@126.com

Abstract: To investigate the plastic deformation (PD) response of a liner material during the shaped-charge jet (SCJ) formation process, the state of motion of liner material and the pattern of change in its deformation environment under explosive loading were theoretically analyzed and modeled. The distribution patterns of the characteristic PD parameters (that is, strain, strain rate, temperature, and flow stress) of the jet at any given time were theoretically predicted. The distribution patterns of the characteristic PD parameters of jets formed from two materials, namely, oxygen-free high-thermal-conductivity copper (OFHC-Cu) and molybdenum (Mo), during their formation process were theoretically analyzed. A series of experimental and numerical simulation studies were conducted to examine the accuracy of the theoretical predictions. As per the results, the developed theoretical model is effective in predicting the one-dimensional distribution of the characteristic PD parameters in the direction of jet formation. At any given time, the distribution of the characteristic PD parameters varies considerably between different parts of the jet. There is no significant difference in the distribution of the strain and strain rate between the jets formed from the two materials in the presence of the same warhead structure. A theoretical analysis predicted average temperatures of 804 and 2277.8 K and average flow stresses of 193.1 and 344.3 MPa for the OFHC-Cu and Mo jets, respectively. A hardness analysis of the jet fragments revealed average strengths of 144.32 and 286.66 MPa for the OFHC-Cu and Mo jets during their formation process, respectively. These results differed by 34% and 20% from the corresponding theoretical predictions.

Keywords: shaped-charge jet; liner; OFHC-Cu; molybdenum; quasi-steady collapse theory; plastic deformation

check for updates

Citation: Song, P.; Li, W.; Liu, J.; Zhang, Q.; Wang, Z. Research on Plastic Flow Characteristic Parameter Distribution of Shaped-Charge Jet: Theory, Experiment, and Simulation. *Appl. Sci.* **2023**, *13*, 5128. https://doi.org/10.3390/app13085128

Academic Editor: Theodore E. Matikas

Received: 14 March 2023
Revised: 7 April 2023
Accepted: 9 April 2023
Published: 20 April 2023

Copyright: © 2023 by the authors. Licensee MDPI, Basel, Switzerland. This article is an open access article distributed under the terms and conditions of the Creative Commons Attribution (CC BY) license (https://creativecommons.org/licenses/by/4.0/).

1. Introduction

Shaped-charge jet (SCJ) warheads are a primary means to strike heavily armored targets. Nonetheless, marked improvements in the passive protection of modern armored targets present a serious challenge for SCJ warheads. Hence, with the aim of further enhancing the armor penetrability, researchers have searched for metal alloys with higher density and plasticity properties that can be used to replace the conventional copper (Cu) liners [1–8].

Bourne [3] studied the jet-formation properties of five pure metallic materials (that is, Cu, silver, zirconium, pure titanium, and depleted uranium) and identified the temperature of a jet as the principal factor affecting its plasticity in his analysis. Lampson [4] prepared conical and trumpet-shaped molybdenum (Mo) liners using powder metallurgy technology combined with forging and forming processes and compared them with Cu liners in terms of the jet-formation performance. Shuai Chen [5] studied the dynamic mechanical properties of pure Mo under the conditions of a high temperature and high strain rate, using the Split Hopkinson pressure bar (SHPB) apparatus, and the plastic deformation behavior of pure Mo under detonation driving was researched experimentally and numerically. Tamer [8] researched the zirconium jet performance by designing different liner shapes. In

addition, numerous studies have shown [7–9] that tungsten (W)-Cu alloys have approximately 30% higher penetration power than red Cu at small standoff distances; however, at a standoff distance of more than three times the caliber, W-Cu jet fracture considerably, resulting in a significantly smaller penetration depth.

In fact, the fracture behavior of the SCJ is primarily affected by its morphology (diameter) and flow stress (strength). Many researchers have investigated the plastic deformation (PD) and fracture behavior of a jet [10–17] and established a large number of engineering and semiempirical models to predict jet fracture times. However, most of these models use the initial strength of the liner material as a substitute for the jet strength, neglecting the effects of the collapse of the liner and the PD history of the jet during the stretching process on the strength of the liner material. Moreover, when driven by a blast pressure as high as 29 GPa, metallic material collapses rapidly at a deformation rate as high as 1×10^5–1×10^6 s^{-1}, leading to marked differences in the distribution of its strain rate, strain, and temperature between different parts of the jet. Therefore, modeling the distribution of the characteristic PD parameters (for example, the strain rate and temperature) of the SCJ is essential for better guiding the design and application of new liner materials and further revealing the intrinsic connections among the warhead structure, material properties, and jet-formation performance.

In this study, based on theories related to the one-dimensional (1D) tensile deformation of SCJ, the distribution of the characteristic plastic flow parameters of the liner material in different parts of a jet at any given time during its deformation process was theoretically modeled. Two materials, namely, oxygen-free high-thermal-conductivity Cu (OFHC-Cu) and Mo, were compared in terms of the distribution patterns of the plastic strain, deformation strain rate, temperature, and flow stress under jet-formation conditions. Experiments and numerical simulations were conducted to examine the accuracy of the theoretical model. Finally, the evolutionary patterns of the microstructure of the two materials before and after deformation were analyzed and discussed.

2. Theoretical Model

2.1. Basic Assumption

The deformation of SCJ is divided into two stages, namely, the collapse and axial stretching of the liner elements. The complex PD of the material during the convergence and collision processes at the axial stagnation points is not considered, while the stratified flow inside the jet is disregarded [18,19]. The total axial PD of a jet element at the given time is assumed to be the sum of its collapse and tensile deformation (that is, 1D simple strain). Figure 1 shows the 1D deformation process of a liner element under this assumption. The red part of the element forms the jet, while the yellow part forms the slug.

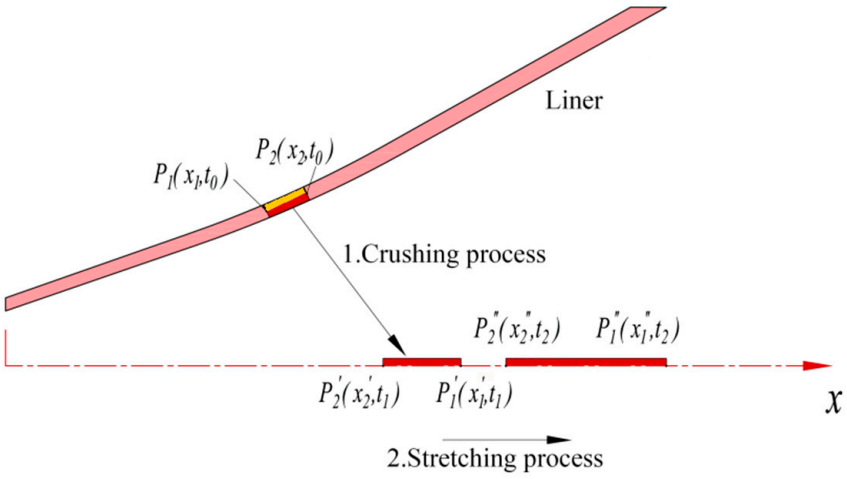


Figure 1. Schematic of the collapse and stretching of a jet element.

2.2. Distribution of the Strain of a Jet

According to the quasi-steady collapse theory of jets, in the Lagrangian coordinate system in Figure 1, the coordinates of the point at which element N moves to collide with the axis at time t_c can be expressed as follows:

$$z(x) = x + y\tan\left(\alpha^N + \delta^N\right). \tag{1}$$

where α is half of the cone angle of the liner and δ is the Taylor angle. Because there is no interaction between the elements, the part of the elements on the axis that forms a jet moves forward at a velocity of V_j. The position of the element in the jet at time t is given below:

$$\xi(x,t) = z(x) + (t - t_c)V_j \quad t \geq t_c. \tag{2}$$

Let $\Delta\xi_0$ and $\Delta\xi$ denote the distance between two points at time t_1 and their increased distance at time t_2, respectively. The 1D tensile strain ε_s of a jet is defined as the ratio of the increase in the length of the element to its initial length. For any x, the following relationship holds:

$$\varepsilon_s(x,t) = \left[\frac{\partial\xi}{\partial x}(x,t)/\frac{\partial\xi}{\partial x}(x,t_0)\right] - 1. \tag{3}$$

Differentiating Equation (2) with respect to x and substituting the result into Equation (3) provides the following equation:

$$\varepsilon_s(x,t) = \frac{(t - t_c(x))V_j'}{z(x)' - t_c(x)'V_j}. \tag{4}$$

In addition, based on the definition of the equivalent strain, the strain ε_c of a liner element during the collapse stage can be expressed as follows:

$$\varepsilon_c(x,t_c) = \frac{\xi(x,t_c(x)) - \xi(x - \Delta x, t_c(x - \Delta x))}{\Delta x/\cos\alpha}(x \geq \Delta x). \tag{5}$$

Therefore, the plastic strain at the time when any jet element collapses on the axis can be determined using Equation (5). Before a fracture, the total strain of any jet element is the sum of Equations (4) and (5).

2.3. Distribution of the Strain Rate of a Jet

Under the basic assumption, the deformation strain rate under jet-formation conditions can be divided into the collapse strain rate and tensile strain rate. Considering the partial derivative of Equation (5) with respect to t yields the 1D tensile strain rate in any part of the jet at any given time:

$$\dot{\varepsilon_s}(x,t) = \frac{\partial\varepsilon_s(x,t)}{\partial t}. \tag{6}$$

To calculate the motion trajectory of the element at any given time, let us consider a point on element N that moves from its initial position $P(x,y)$ to $P'(x',y')$ at time t. The coordinates of point P' (as shown in Figure 1) can be expressed as follows [20,21]:

$$\begin{cases} x' = x + \int_{T^N}^{t} V^N(\tau)\sin\left[\alpha^N + \delta^N(\tau)\right]d\tau \\ y' = y - \int_{T^N}^{t} V^N(\tau)\cos\left[\alpha^N + \delta^N(\tau)\right]d\tau \end{cases}. \tag{7}$$

Equation (7) can be used to calculate the deformation time $\Delta t(x)$ of any liner element, that is, the time between the start of its collapse and its arrival on the axis. The collapse strain

rate $\dot{\varepsilon_c}$ of the element is defined as the ratio of its collapse deformation to its deformation time and therefore can be expressed as follows:

$$\dot{\varepsilon_c}(x) = \frac{\varepsilon_c(x, t_c)}{\Delta t(x)}. \tag{8}$$

2.4. Distribution of the Temperature of a Jet

The increase in the temperature of a jet could be primarily ascribed to the heat generated from two sources, namely, the work done by the PD of the material and the compression of the explosive shock wave [22]. Therefore, the temperature rise due to each of these two sources needs to be calculated separately.

2.4.1. Adiabatic Temperature Rise

The deformation stress of most metallic materials depends primarily on its strain history, deformation strain rate, and deformation temperature [23]. In other words, the equivalent stress of a material can be simply expressed as follows:

$$\sigma = f(\varepsilon, \dot{\varepsilon}, T). \tag{9}$$

Equation (9) is referred to as the constitutive equation of material deformation. Due to the differences in the material's properties as well as research methods and perspectives, Equation (9) has many functional forms. The Johnson–Cook (J–C) [24] constitutive equation, as shown in Equation (10), is used in this study to calculate the flow stress of the SCJ.

$$\sigma = (A + B\varepsilon_p^n)(1 + C ln\dot{\varepsilon}^*)(1 - T^{*m}), \tag{10}$$

where A, B, n, C, and m are the constitutive parameters of the material to be determined, $\dot{\varepsilon}^* = \frac{\dot{\varepsilon}}{\dot{\varepsilon}_0}$(where $\dot{\varepsilon}_0$ is the reference strain rate), and $T^* = \frac{(T-T_r)}{(T-T_m)}$ (where T_r is the reference temperature and T_m is the melting point of the material). The rise in the material's temperature due to the work done by PD can be calculated using the following equation [25]:

$$\Delta T(\varepsilon) = \frac{\beta}{\rho C_v} \int_0^{\varepsilon} \sigma d\varepsilon, \tag{11}$$

where ρ is the density of the material, C_v is the specific heat of the material, and β is the thermal conversion coefficient, that is, the ratio at which plastic work is converted into heat (β is set to 0.9 in the calculations in this study). Substitution of Equation (10) into Equation (11) provides the following equation:

$$\int_{T_0^*}^{T_1^*} \frac{dT^*}{1 - T^{*m}} = \frac{0.9\left(1 + C ln\dot{\varepsilon}/\dot{\varepsilon}_0\right)}{\rho C_V} \int_0^{\varepsilon} (\sigma + B\varepsilon^n) d\varepsilon. \tag{12}$$

A numerical calculation based on Equation (12) yields the material temperature rise due to PD, ΔT_1.

2.4.2. Shock-Induced Temperature Rise

In the jet-formation process, a shock wave with a pressure of up to 40 GPa can be formed inside the liner material at the instant when the blast wave formed after the detonation of the explosive acts on the liner [26]. The compressive action of the powerful shock wave leads to an increase in the internal temperature of the material. The rise in the material's temperature due to the shock wave, ΔT_s, can be calculated using the following equation [16]:

$$\Delta T_s = T_0 exp\left[\frac{\gamma_0}{v_0}(v_0 - v_1)\right] + \frac{P(v_0 - v_1)}{2C_V} + \frac{exp\left[\frac{\gamma_0 v_1}{v_0}\right]}{2C_V} \int_{v_0}^{v_1} Pexp\left(\frac{\gamma_0 v_1}{v_0}\right)\left[2 - \frac{\gamma_0}{v_0}(v_0 - v_1)\right] dv, \tag{13}$$

where P is the peak pressure of the shock wave, v_0 is the initial specific volume of the material, and v_1 is the post-wave specific volume of the material, which can be calculated using the following equation:

$$v_1 = \frac{C_0^2}{2PS^2}\left[\sqrt{1+\frac{4PSv_0}{C_0^2}}+\frac{2S(S-1)v_0P}{C_0^2}-1\right], \tag{14}$$

where C_0 and S are the relationship constants of the shock-wave velocity U_s and the particle velocity U_p, respectively. The shock wave is immediately followed by a rarefaction wave. The action of the rarefaction wave leads to a decrease in the temperature of the material. The residual temperature of the material after the action of the rarefaction wave, ΔT_2, is calculated as follows [22]:

$$\Delta T_2 = \Delta T_s exp\left[\frac{\gamma_0}{v_0}(v_s - v_0)\right], \tag{15}$$

where v_s is the specific volume of the shocked material. Therefore, the rise in the material's temperature at any given time ($t \leq t_b$) during the jet-formation process can be expressed as follows:

$$\Delta T = \Delta T_1 + \Delta T_2. \tag{16}$$

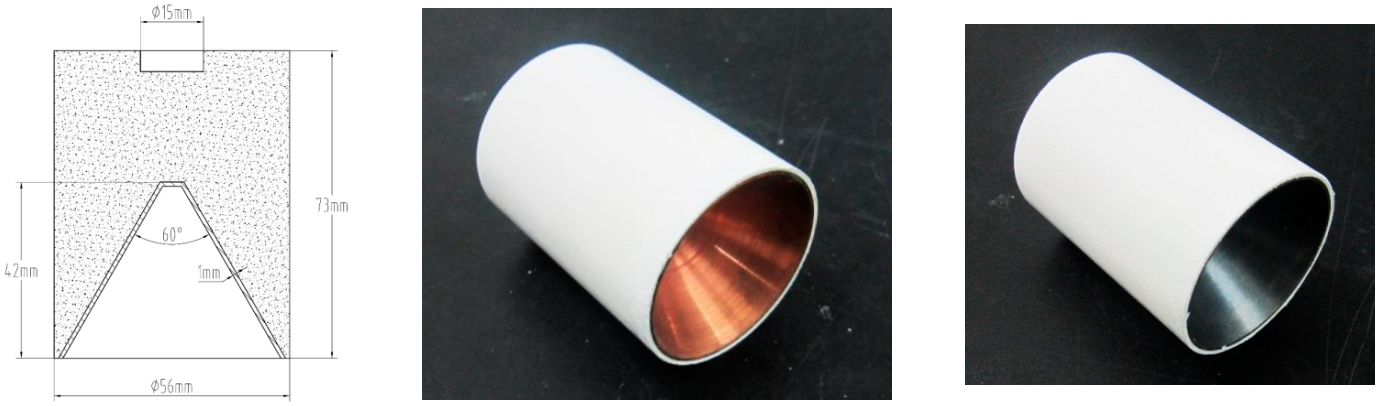
Substituting Equations (5)–(8) and (16) into the constitutive model provides the distribution of the temperature of the SCJ at any given time.

3. Plastic Flow Characteristics of OFHC-Cu and Mo Jets

Based on a specific warhead structure, a combination of experimental and numerical simulation studies was conducted to compare the deformation characteristics of the SCJ formed from OFHC-Cu and pure Mo liners when driven by explosive loading.

3.1. Relevant Parameters of the Warhead

The warhead used in the experiment featured a caliber of 56 mm and a charge height of 73 mm and was filled primarily with the 8701 (JH-2) press-loaded charge with a density of 1.68 g/cm^3. With a cone angle of 60° and a wall thickness of 1 mm, both liners were prepared by machining the bar stock of the corresponding materials, as shown in Figure 2.



(**a**) (**b**) (**c**)

Figure 2. SCJ warhead. (**a**) Dimensions of the warhead; (**b**) OFHC-Cu liner; (**c**) Pure Mo liner.

3.2. Experimental Studies

3.2.1. Pulsed X-ray Experiment

In this study, a multi-pulse X-ray photography system was used to capture the spatial positions of the jets formed from both the OFHC-Cu and pure Mo liners at any two time points after charge detonation, with the aim of determining the morphology and velocity distribution patterns of the two jets. Figure 3 shows the experimental layout.

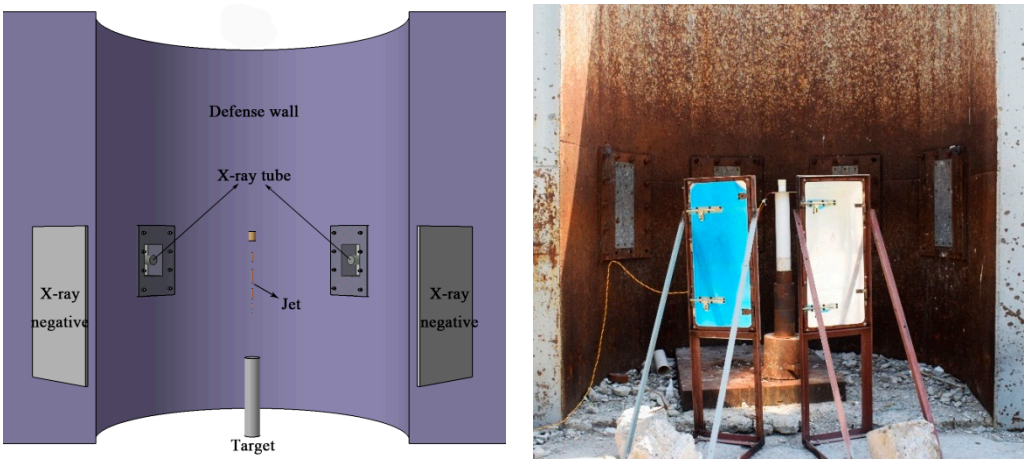


Figure 3. Pulsed X-ray experiment. (**a**) Schematic of the experimental layout; (**b**) Layout at the experimental site.

3.2.2. Partial Jet Recovery Experiment

A water medium was used to recover the jets formed from the two materials. During the experiment, #45 steel was used to pre-consume the high-velocity part of each jet that could not be easily recovered in its entirety, after which a water medium was used to decelerate and recover the subsequent low-velocity part of the jet. Figure 4 shows the recovery setup used in the experiment and the layout of the experimental site.

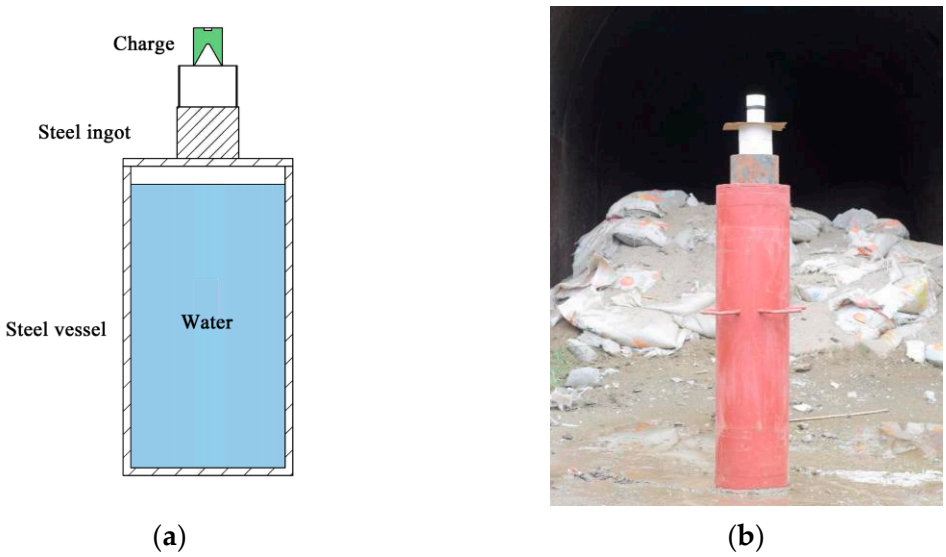


Figure 4. Layout of the site of the SCJ recovery experiment. (**a**) Schematic of the experimental setup; (**b**) Experimental site.

3.3. Numerical Simulations

To determine the distribution patterns of the temperature of the jets formed from the two materials during their formation process and to examine the accuracy of the jet temperatures predicted by the theoretical model, the formation process of each of the OFHC-Cu and Mo SCJs was numerically simulated using the Autodyn-2D finite element (FE) software (Anasys 14.0). Figure 5 shows the developed two-dimensional axisymmetric FE model. To improve the computational efficiency, the grid cell size of the air domain was set to 0.25 mm × 0.25 mm. Table 1 summarizes the main material parameters used in the numerical simulations.



Figure 5. Computational simulation model.

Table 1. Main material parameters of the numerical model.

JH-2 [27]	ρ (g/cm^3)	D (m/s)	P_{CJ} (GPa)	A (GPa)	B (GPa)	R_1	R_2	ω	E_0 (GPa)	V_0
	1.71	8212	29.6	854.5	20.493	4.6	1.35	0.25	10.0	1.0
OFHC-Cu [28]	ρ (g/cm^3)	G (GPa)	Tm (K)	A (GPa)	B (GPa)	n	C	m	C_0 (m/s)	S_1
	8.96	47.7	1356	0.09	0.292	0.31	0.02	1.09	3940	1.49
	S_2	S_3	γ_0	E	V_0	C_p (J/gK)				
	0.6	0	1.99	0	1.0	383				
Mo [29,30]	ρ (g/cm^3)	G (GPa)	Tm (K)	A (GPa)	B (GPa)	n	C	m	C_0 (m/s)	S_1
	10.03	131	3660	0.3	0.32	0.3	0.07	1	5124	1.232
	S_2	S_3	γ_0	E	V_0	C_p (J/gK)				
	0	0	1.52	0	1.0	243				

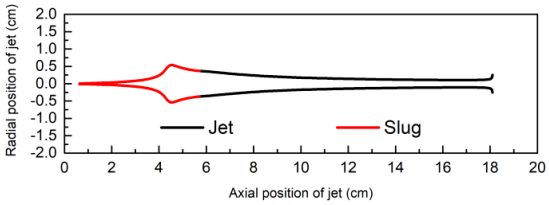
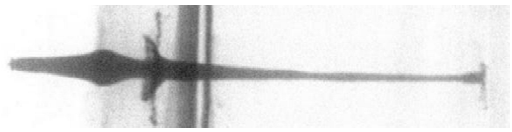
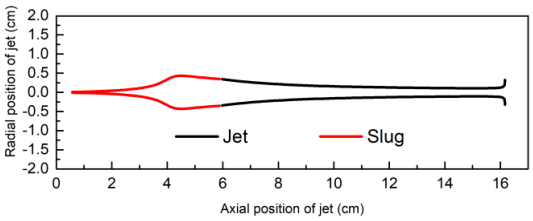
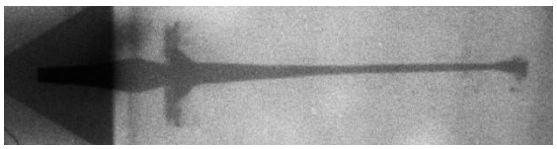
4. Results and Discussion

4.1. Jet Morphology

The morphology (length and diameter) and head and tail velocities of the SCJ formed from the two materials at identical time points were calculated through numerical simulations and the theoretical model, respectively. The results are compared with those obtained from the X-ray experiment.

As shown in Table 2, the profiles of the OFHC-Cu and Mo jets predicted by the theoretical model at the given time are consistent with the numerical simulations and experimental data. The head and slug velocities of the jet formed from each material predicted by the theoretical model differed by less than 5% and 12% from the experimental data, respectively. Overall, the theoretical calculation model was effective in yielding accurate predictions for the tensile motion of the jet.

Table 2. Comparison of jet morphology.

Material		Jet Morphology	Head Velocity (m/s)	Slug Velocity (m/s)
OFHC-Cu (34 μs)	Theoretical calculations		6610	1068
	Numerical simulations		6519	923
	Experimental results		6498	961
Mo (32 μs)	Theoretical calculations		6345	863
	Numerical simulations		6461	827
	Experimental results		6421	925

4.2. Strain Distribution of the Jets

Figure 6 shows the 1D distribution relationship between the elements of the OFHC-Cu jet and their initial positions at different times, as obtained using the theoretical model. After the detonation of the charge, the elements located in the topmost part of the liner were the first to move toward the axis. However, due to their small distances from the axis, the top elements could not be accelerated to the ultimate collapse velocity after the collapse and therefore converged and separated on the axis. Consequently, the jet elements formed from the topmost part of the material moved at a lower velocity than those behind them.

Figure 7 shows the theoretically calculated distribution patterns of the collapse strain of the OFHC-Cu jet and its total strain on the axis of the liner at different time points after the collapse. It is evident that the maximum collapse strain of some of the liner elements already reached 7 when they collapsed onto the axis. After the elements collapsed onto the axis, the total strain in the other parts of the liner gradually increased as the tensile motion of the jet further developed.

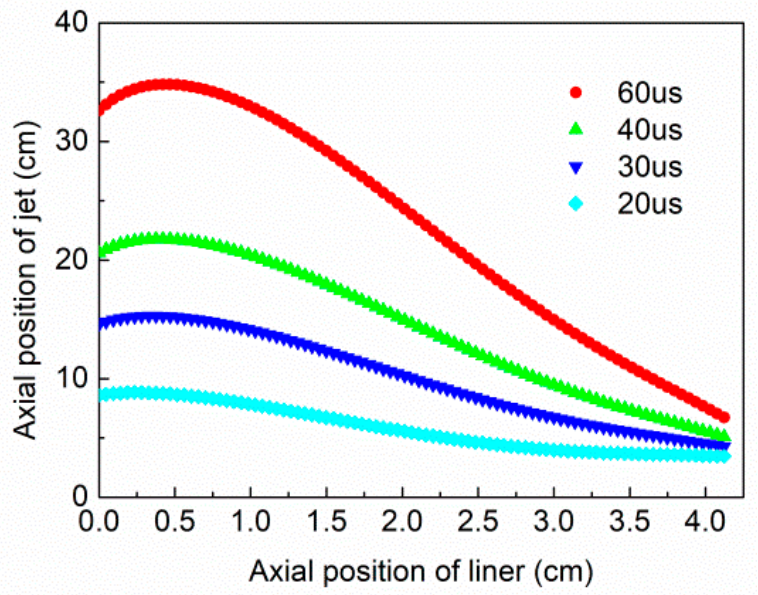


Figure 6. Tensile motion of the jet.

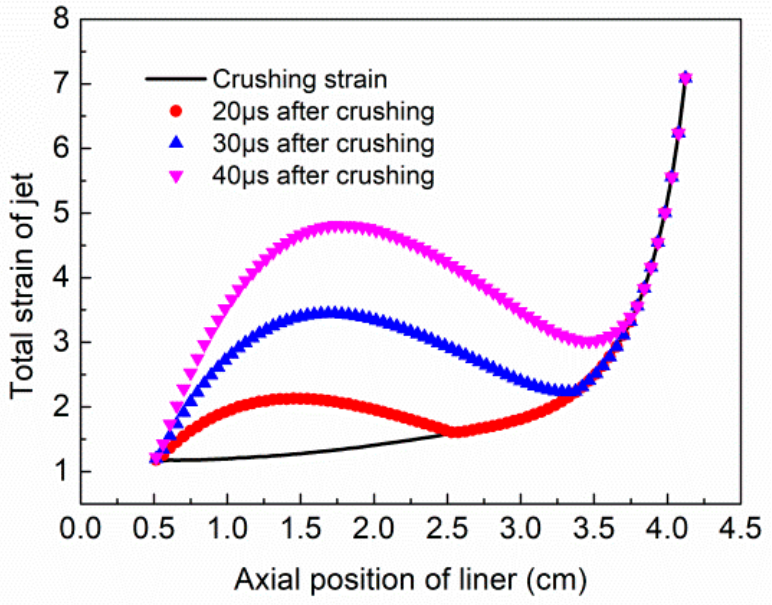


Figure 7. Total strain of the jet.

Figure 8a,b show the theoretically calculated and numerically simulated distribution patterns of the strains of the jets formed from the OFHC-Cu and Mo liners 40 μs after detonation, respectively. The analysis revealed no significant difference in the distribution of the strain between the jets formed from the liners made of the two materials in the presence of the same warhead structure. Compared with the theoretical model, numerical simulations were effective in predicting the distribution of the strain in the direction transverse to the stretching direction of each jet. At 40 μs, the average strains at the heads of the OFHC-Cu and Mo jets were 5.62 and 5.37, respectively. As shown in Figure 8a, the maximum strains at the heads of the two jets predicted by the theoretical model were 4.86 and 4.58, respectively. The primary reason that the theoretical predictions are lower than the numerical simulation results is that the theoretical model only considers the plastic strain accumulation during the collapse and 1D tensile motion of the jet, while neglecting the stratified flow inside the jet material.

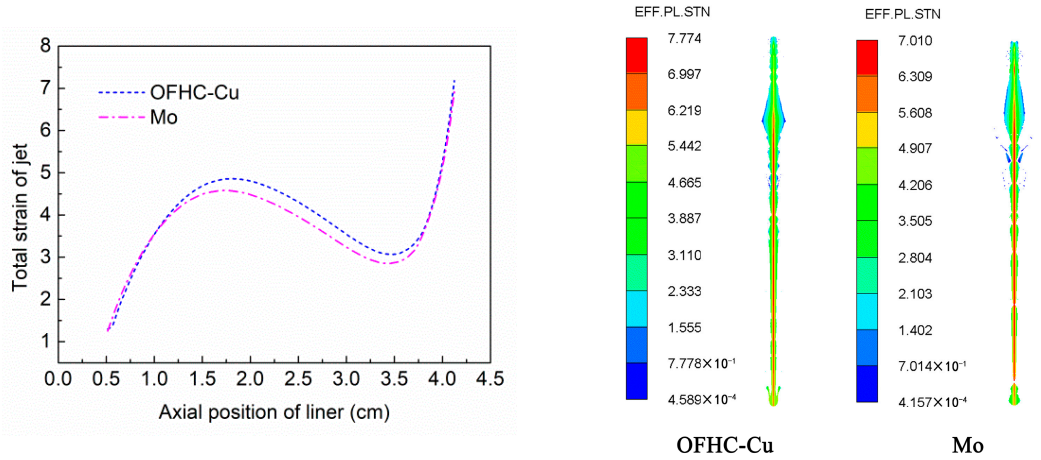


Figure 8. Strain distribution of the OFHC-Cu and Mo jets (at 40 μs). (**a**) Theoretical predictions; (**b**) Numerical simulations.

4.3. Strain-Rate Distribution of the Jets

Figure 9a,b show the theoretically calculated distribution patterns of the deformation strain rates of the OFHC-Cu and Mo jets during collapse and stretching (at 40 μs), respectively. Overall, the deformation strain rates of the materials during the collapse process ranged primarily from 7×10^4 and 1.6×10^5 s^{-1}. Compared with the collapse process, the tensile strain rates of the two jets were considerably lower in the stretching process, ranging from 8×10^3 to 8.4×10^4 s^{-1}.

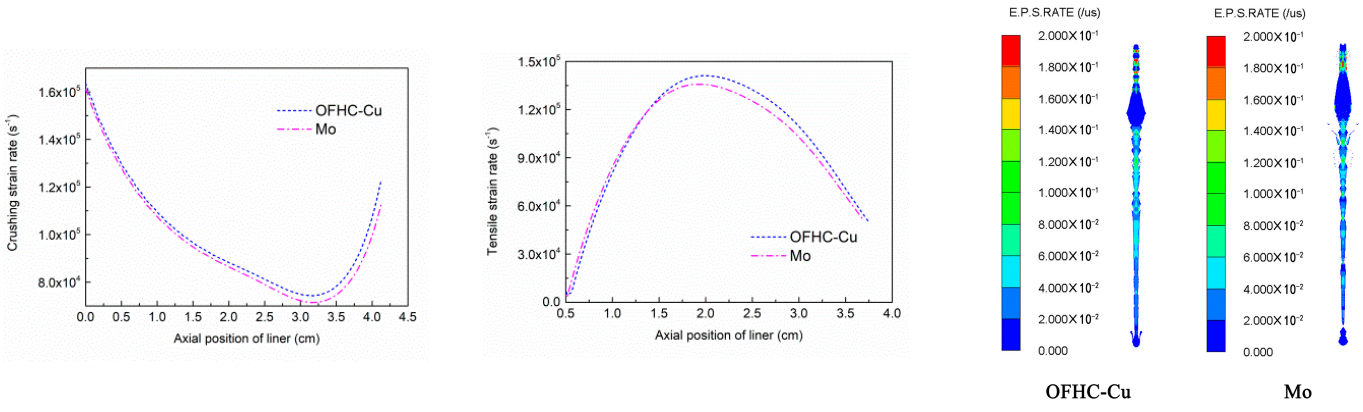


Figure 9. Strain-rate distribution of the OFHC-Cu and Mo jets. (**a**) Collapse strain rates; (**b**) Tensile strain rates (at 40 μs); (**c**) Numerical simulations (at 40 μs).

Figure 9c shows a numerically simulated diagram of the strain-rate distribution of each of the two jets 40 μs after detonation. To facilitate analysis and comparison, the numerically simulated deformation strain rates of the materials at different positions on the axis of each jet were averaged and compared with the theoretical calculation results. As shown in Table 3, the theoretically calculated values of the 1D tensile deformation strain rates of the jets were greater than their numerically simulated values.

Table 3. Distribution of the deformation strain rate of each jet at 40 μs and data comparison.

Material	Numerically Simulated Strain-Rate Distribution of the Jet (s^{-1})						Average (s^{-1})	
	13 cm	15 cm	17 cm	19 cm	21 cm	24 cm	Numerical Simulation	Theoretical Calculation
OFHC-Cu	4.5×10^4	4.4×10^4	3.6×10^4	5.1×10^4	3.1×10^4	3.0×10^4	4.0×10^4	6.2×10^4
Mo	4.8×10^4	9.2×10^4	2.8×10^4	2.8×10^4	3.6×10^4	5.0×10^4	4.7×10^4	6.0×10^4

4.4. Temperature Distribution of the Jets

Figure 10a,b show the theoretically calculated and numerically simulated temperature distribution patterns of the OFHC-Cu and Mo jets at 40 μs, respectively. Similar to its strain, the temperature of each jet also exhibited a stratified distribution pattern. The temperature of the material gradually decreased from the center along the radial direction of each jet and was the highest at the center of the jet.

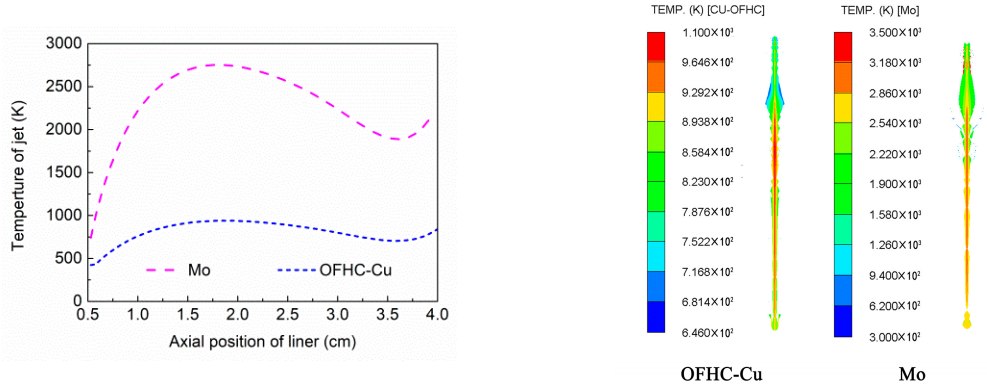


Figure 10. Temperature distribution of the OFHC-Cu and Mo jets (at 40 μs). (**a**) Theoretical predictions; (**b**) Numerical simulations.

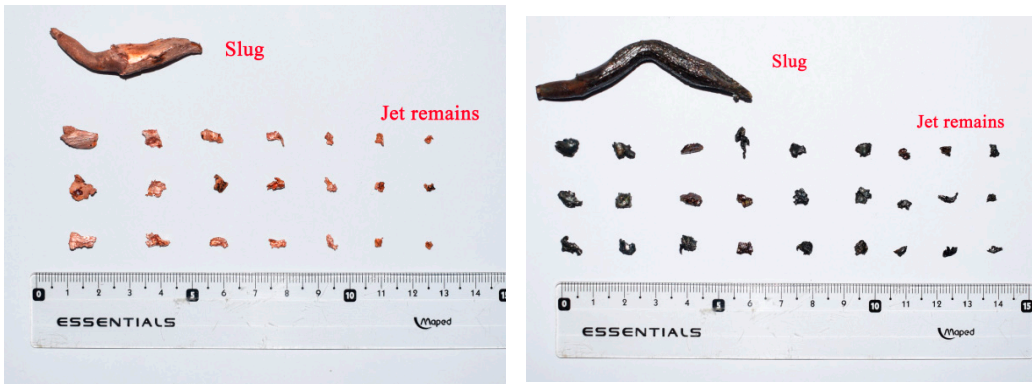
To facilitate comparative analysis, the temperatures of the material at 40 μs were extracted from a total of 10 test points, forming the array composed of five columns and two rows along the movement and radial directions of each jet, and were subsequently averaged and compared with the theoretical calculation results. Table 4 summarizes the results. Evidently, the temperatures of the Mo jet were appreciably higher than those of the OFHC-Cu jet. The numerical simulations yielded average temperatures of 873.2 and 2826.9 K for the OFHC-Cu and Mo jets, respectively. The theoretical model predicted average temperatures of 804 and 2277.8 K for the two jets at the same time point, respectively. The theoretical predictions did not differ significantly from the numerical simulation results.

Table 4. Temperature distribution of the jets at 40 μs and data comparison.

Material	Numerically Simulated Temperature Distribution of the Jet (K)					Average Temperature (K)	
						Numerical Simulation	Theoretical Calculation
OFHC-Cu	811.7	879.2	859.6	738.4	767.5	873.2	804.0
	928.7	931.5	1012.0	916.2	893.4		
Mo	2718.2	2760.5	2711.5	2552.8	2702.3	2826.9	2277.8
	3076.3	3040.1	2905.3	2899.2	2894.7		

4.5. Hardness and Strength of the Jets

Figure 11 shows the fragments and slugs of the SCJ formed from the two materials that are obtained from the underwater recovery experiment. In total, 18.7 g (46.8%) of the OFHC-Cu jet was recovered, of which the slug accounted for 15.68 g. In comparison, 27.9 g (61.2%) of the Mo jet was recovered in total, of which the slug accounted for 24.2 g.



(**a**) (**b**)

Figure 11. Recovered jet fragments and slugs. (**a**) OFHC-Cu; (**b**) Mo.

Seven recovered fragments of each of the OFHC-Cu and Mo jets were selected and analyzed using a hardness tester to determine their hardness. The results were averaged to yield the average hardness for each jet. As shown in Table 5, the recovered OFHC-Cu and Mo jet samples exhibited the average hardness of 571.61 and 2119.99 MPa, respectively. The hardness of the Mo jet fragments was approximately 3.7 times that of the OFHC-Cu jet fragments.

Table 5. Hardness of the jets.

Material	Hardness of Different Jet Particles (MPa)							Average (MPa)
OFHC-Cu	514.86	546.25	658.05	557.03	494.27	701.20	529.57	571.60
Mo	1992.78	2107.52	2174.21	2085.94	1948.65	2279.14	2251.68	2119.99

Research [31] has shown that the hardness of most metallic materials is approximately three times their yield strength. On this basis, the yield strengths of the fragments of the two jets can be estimated to be 190.53 and 706.66 MPa, respectively. However, these values were only the yield strengths of the jet fragments at the completion of the experiment. Determining the yield strength of each material during the jet-formation process requires taking into consideration the stress softening caused by the high temperature of the material during this process.

Based on the specific form of the J–C constitutive equation, the amount of stress softening due to the material temperature rise, $\Delta\sigma_T$, can be expressed as follows:

$$\Delta\sigma_T = A\left(\frac{T - T_r}{T_m - T_r}\right)^m. \quad (17)$$

Because the cooling process of jet particles is unaffected by the strain-rate effect, the relationship between the yield strength of the material and the ambient temperature under quasi-static deformation conditions can be used to fit the correlation coefficient in Equation (17) to obtain a mathematical relationship between the amount of stress softening of the material and the ambient temperature. Furthermore, the strength of each jet can be estimated from the strength data for its fragments. Table 6 summarizes the results and the relevant parameters. As shown in Table 6, the OFHC-Cu and Mo jets exhibited average

strengths of 144.32 and 286.66 MPa after a fracture (that is, after the end of PD), respectively. The average strength of the Mo jet was approximately twice that of the OFHC-Cu jet.

Table 6. Jet strength estimates.

Material	Model Parameters				T_j (K)	Jet Strength (MPa)
	A (MPa)	m	T_r (K)	T_m (K)		
OFHC-Cu [24]	90	1.09	300	1356	873	144.32
Mo [32]	441.25	0.1774	226	3660	2826	286.66

Figure 12 shows the theoretically calculated flow-stress distribution of each of the OFHC-Cu and Mo jets after a fracture. It is evident that the flow stress varied considerably between the elements in different parts of each jet due to the deformation environment. Overall, the flow stress of the Mo jet was significantly higher than that of the OFHC-Cu jet. From the head to the tail of each jet, the flow stress of the elements first decreased and thereafter increased, with the minimum value occurring at $\frac{1}{3}$ of the distance from the head of the jet. The average flow stresses of the elements in the low-velocity (2000–4500 m/s) parts of the OFHC-Cu and Mo jets were 193.1 and 344.3 MPa, respectively. These values differ by 34% and 20% from the jet strength estimates in Table 6, respectively.

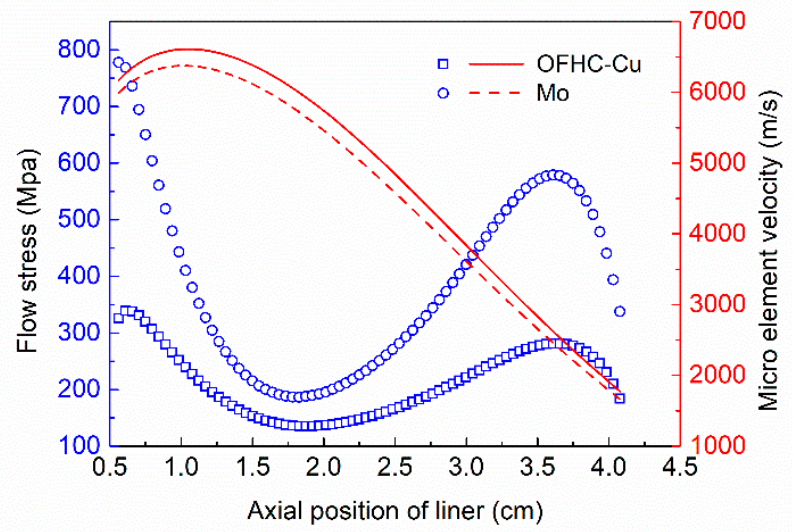


Figure 12. Flow-stress distribution of the jets.

4.6. Microstructural Evolution

A metallurgical microscope was used to observe the microstructure of the OFHC-Cu and Mo jets obtained from the recovery experiment to analyze the microstructural evolution of the two materials during the jet-formation process.

Figure 13 shows the microstructural morphology of OFHC-Cu before and after jet formation ((a): microstructure of the OFHC-Cu liner; (b–d): microstructural morphology of different parts of the slug of the jet; (e,f): microstructural morphology of the jet). The analysis revealed that compared with that before jet formation, OFHC-Cu decreased considerably in the crystal grain size and exhibited notable microstructural flow characteristics after the formation of a jet. This phenomenon suggests that driven by explosive loading, the liner material underwent dynamic recrystallization, during which the initial coarse crystals were crushed and reorganized, resulting in the formation of a large number of equiaxed fine crystals.

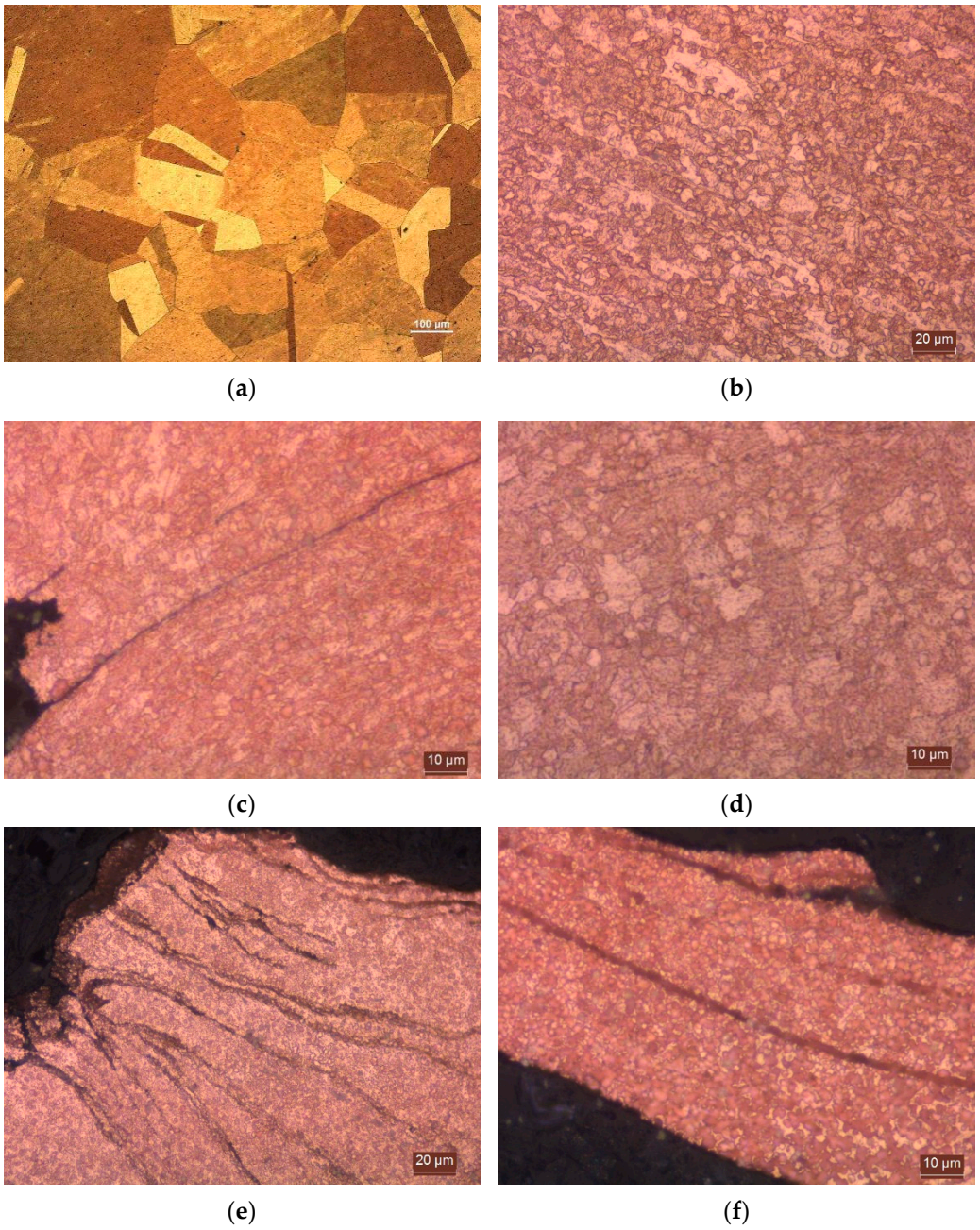
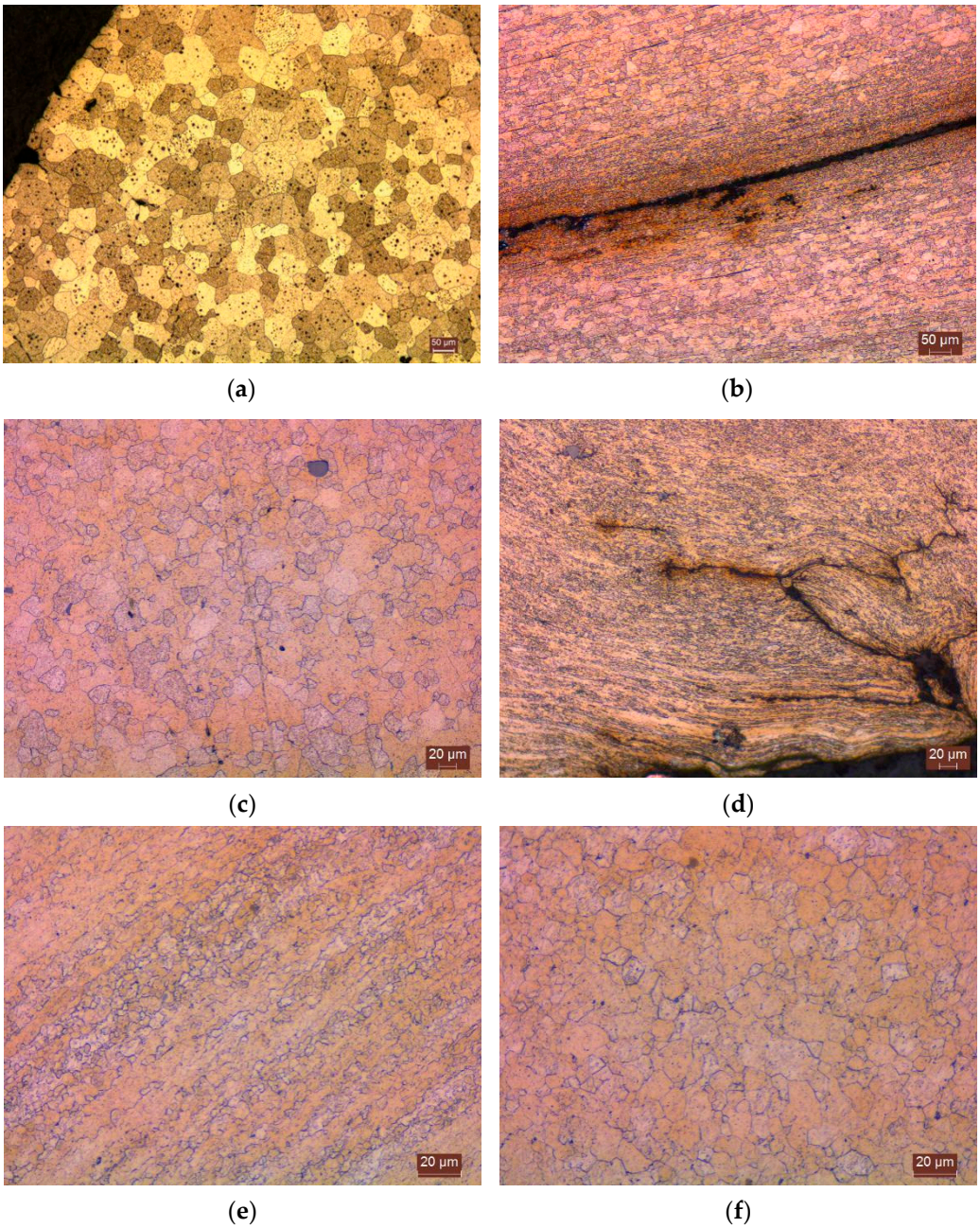


Figure 13. Microstructural morphology of OFHC-Cu. (**a**) Initial structure; (**b**–**d**) Slug structure; (**e**,**f**) Jet structure.

A comparison of Figure 13b–f revealed that the crystal grains in the OFHC-Cu slug ranged from 1.3 to 8.51 μm in size, with the average size of 3.4 μm, whereas the crystal grains in the OFHC-Cu jet particles ranged from 0.84 to 3.6 μm in size, with the average size of 2.4 μm. The jet exhibited a smaller grain size and contained a larger number of fine crystals than the slug, suggesting more significant deformation and a higher degree of dynamic recrystallization in the material in the jet than in the slug. Moreover, the deformed OFHC-Cu structure contained a large number of concentrated deformation zones (Figure 13c,e,f), around which the structure exhibited a smaller grain size (Figure 13c).

Figure 14a shows the microstructure of the Mo liner; Figure 14b,c show the microstructural morphology of different parts of the slug; and Figure 14d–f show the microstructural morphology of the jet. The analysis revealed that similar to OFHC-Cu, Mo also underwent dynamic recrystallization during the jet-formation process. The slug exhibited the

average crystal grain size of 23.4 μm. The material in the jet underwent a higher degree of recrystallization, with the average grain size of 7.8 μm. Compared with OFHC-Cu, the fully recrystallized Mo jet exhibited a larger crystal grain size, resulting in a relatively low coordinated PD capacity. A large number of macroscopic cracks (10–20 μm in width) formed due to the concentrated deformation were found in the microstructure of the Mo slug and jet (Figure 14b,d).



(**a**) (**b**) (**c**) (**d**) (**e**) (**f**)

Figure 14. Microstructural morphology of Mo. (**a**) Initial structure; (**b**,**c**) Slug structure; (**d**–**f**) Jet structure.

5. Conclusions

In this study, a theoretical model was developed to calculate the distribution of the characteristic plastic flow parameters of an SCJ. This model can be used to theoretically predict the distribution patterns of the strain, strain rate, temperature, and flow stress of the jet formed from the liner made of any material and of any shape at any given time during its

formation process. Jets formed from OFHC-Cu and Mo were comprehensively compared in terms of their PD behavior through theoretical analysis, numerical simulations, and experimental investigations. The results of this study are as follows:

(1) The developed theoretical model was effective in predicting the PD behavior of the SCJ and the distribution patterns of the relevant characteristic parameters. Comprehensive analysis revealed that the PD environment of the material varied considerably between different parts of a jet during its formation.

(2) At any given time point, the distribution of the plastic strain differed considerably in both the longitudinal and transverse directions of a jet, with the most intensive material occurring at the center. The deformation strain rates of the liner materials during the collapse stage were theoretically predicted to range from 0.8×10^5 to 1.6×10^5 s^{-1}. The distribution patterns of the strain and strain rate of a jet were affected primarily by the warhead structure. In the presence of the same warhead structure, the two materials did not differ considerably in terms of the distribution of the strain and strain rate.

(3) The average temperatures of the OFHC-Cu and Mo jets 40 μs after detonation were theoretically predicted to be 804 and 2277.8 K, respectively. These results agreed adequately with the numerical simulation results. The measurements obtained in the recovery experiment revealed average strengths of 144.32 and 286.66 MPa for the OFHC-Cu and Mo jets, respectively. The theoretical model predicted flow stresses of 193.1 and 344.3 MPa for the two jets, respectively. These two sets of data differed numerically by 34% and 20%, respectively.

(4) Both materials underwent dynamic recrystallization to varying degrees during the jet-formation process. In both cases, the material was more intensively recrystallized in the jet than in the slug. Moreover, the crystal grain size of the Mo jet decreased from the initial 44.7 μm to 7.82 μm, whereas the crystal grain size of the OFHC-Cu jet decreased from the initial 95.6 μm to 2.2 μm.

Author Contributions: Conceptualization, W.L.; Methodology, P.S.; Validation, J.L. and Q.Z.; Resources, W.L. and Q.Z.; Data curation, P.S.; Writing—original draft, P.S.; Writing—review & editing, Z.W.; Supervision, J.L. All authors have read and agreed to the published version of the manuscript.

Funding: This research received no external funding.

Institutional Review Board Statement: The study did not require ethical approval.

Informed Consent Statement: The study did not involve humans.

Data Availability Statement: Data is unavailable due to privacys.

Conflicts of Interest: The authors declare no conflict of interest.

References

1. Laszlo, J.K.; William, P.W. Investigation of a Bulk Metallic Glass as a Shape Charge Liner Material. In Proceedings of the 23rd International Symposium of Ballistics, Tarragona, Spain, 16–20 April 2007.
2. Saran, S.; Ayisit, O.; Yavuz, M.S. Experimental Investigations on Aluminum Shaped Charge Liners. *Procedia Eng.* **2013**, *58*, 479–486. [CrossRef]
3. Bourne, B.; Cowan, K.G.; Curtis, J.P. Shaped Charge Warheads Containing Low Melt Energy Metal Liners. In Proceedings of the 19th International Symposium of Ballistics, Interlaken, Switzerland, 7–11 May 2001; pp. 583–590.
4. Lampson, M.L.; Summers, R.L. *Determination of the Yield Strength of a Molybdenum Jet*; Army Research Laboratory: Adelphi, MD, USA, 1998.
5. Chen, S.; Li, W.-B.; Wang, X.-M.; Yao, W.-J. Explosion/impact response of pure molybdenum at ultra-high strain rate and large strains. *Int. J. Refract. Met. Hard Mater.* **2022**, *104*, 105801. [CrossRef]
6. Wang, T.; Ruan, W.; Zhu, H. Depleted uranium liner and thier shaped energy jets. *Explos. Shock.* **1995**, *2*, 180–184.
7. Hamidi, A.G.; Arabi, H.; Rastegari, S. Tungsten–copper composite production by activated sintering and infiltration. *Int. J. Refract. Met. Hard Mater.* **2011**, *29*, 538–541. [CrossRef]
8. Lasilla, D.H. Mechanical behaviour of tungsten shaped charge liner material. In Proceedings of the 14th Symposium on Ballistics, Quebeck, QC, Canada, 26–29 September 1993; Volume 2, pp. 145–153.

9. Winer, K.A.; Breithaup, R.D.; Muelder, S.A.; Baum, D.W. High-resolution observations of tungsten liner collapse and early jet formation. In Proceedings of the 16th International Ballistic Symposium, San Francisco, CA, USA, 23–28 September 1996; Volume 2, pp. 439–448.
10. Shwartz, A.J.; Baker, E.L. Effect of interior surface finish on the break-up of copper shaped charge. In Proceedings of the 18th International Ballistic Symposium, San Antonio, TX, USA, 15–19 November 1999; Volume 2, pp. 559–566.
11. Winer, K.A.; Breithaup, R.D.; Muelder, S.A.; Baum, D.W. High-speed, high-resolution observations of shaped-charge jets undergoing particulation. In Proceedings of the 15th International Ballistic Symposium, Jerusalem, Israel, 21–24 May 1995; Volume 2, pp. 89–96.
12. Hirsh, E. Internal shearing during shaped charge jet formation and break-up. *Prop. Expl. Pyrotechn.* **1992**, *17*, 27–33. [CrossRef]
13. Lichtenberger, A. The influence of grain size and quality of nickel based liners on the ductility of shaped charge jet. In Proceedings of the 13th Symposium on Ballistics, Stockholm, Sweden, 1–3 June 1992; Volume 2, pp. 377–384.
14. Elshenawy, T.; Li, Q.M.; Elbeih, A. Experimental and numerical investigation of zirconium jet performance with different liner shapes design. *Def. Technol.* **2022**, *18*, 12–26. [CrossRef]
15. Wang, Z.; Li, X.; Zhang, C.; Yi, C.; Wang, H.; Sun, W. Explosive consolidation of W-Cu alloy as liner material and its properties. *Explos. Shock.* **2011**, *31*, 332–336.
16. Chou, P.C. The stability of shaped-charge jets. *J. Appl. Phys.* **1977**, *48*, 4187–4195. [CrossRef]
17. Haugstad, B. On the Break-Up of Shaped Charge Jets. *Propellants Explos. Pyrotech.* **1983**, *8*, 119–120. [CrossRef]
18. Ouyang, C. Research on fracture jet. *Acta Armamentarii* **1985**, *2*, 32–38.
19. Dou, J.-H.; Jia, X.; Huang, Z.-X.; Gu, X.H.; Zheng, Y.M.; Ma, B.; Xiao, Q.Q. Theoretical and numerical simulation study on jet formation and penetration of different liner structures driven by electromagnetic pressure. *Def. Technol.* **2022**, *17*, 846–858. [CrossRef]
20. Ma, B.; Huang, Z.-X.; Guan, Z.-W.; Jia, X.; Zu, X.D.; Xiao, Q.Q. Investigate the effects of magnetic fields on the penetration ability of a shaped charge jet at different standoffs. *Def. Technol.* **2021**, *17*, 1722–1730. [CrossRef]
21. Zheng, Z. Stability of shaped energy jet. *Explos. Shock.* **1981**, *1*, 6–17.
22. Tao, G.; Chen, H.; Shen, Q. Superplasticity flow problems of copper shaped-charge jet. *Explos. Shock.* **2008**, *28*, 336–340.
23. Perzyna, P. Application of the Thermodynamical Theory of Elasto-Viscoplasticity in Modern Manufacturing Processes. In *Damage Mechanics and Micromechanics of Localized Fracture Phenomena in Inelastic Solids*; CISM Courses and Lectures; Springer: Vienna, Austria, 2011; Volume 525, pp. 227–376.
24. Gr, J.; Wh, C. A constitutive model and data for metals subjected to large strains, high strain rates and high temperatures. In Proceedings of the 7th International Symposium on Ballistics, Hague, The Netherlands, 19–21 April 1983; pp. 541–548.
25. Kapoor, R.; Nemat-Nasser, S. Determination of temperature rise during high strain rate deformation. *Mech. Mater.* **1998**, *27*, 1–12. [CrossRef]
26. Chen, H. Study on Dynamic Deformation of Shaped Metal Jet during Formation and Penetration. Nanjing University of Science and Technology: Nanjing, China, 2011.
27. Cao, B.Y.; Lassila, D.H.; Schneider, M.S.; Kad, B.K.; Huang, C.X.; Xu, Y.B.; Kalantar, D.H.; Remington, B.A.; Meyers, M.A. Effect of shock compression method on the defect substructure in monocrystalline copper. *Mater. Sci. Eng. A* **2005**, *409*, 270–281. [CrossRef]
28. Li, R. Study on the Detonation of Charge under Multipoint Initiation and the Forming Mechanism of Rod Penetrator. Nanjing University of Science and Technology: Nanjing, China, 2020.
29. Kleiser, G.; Revil-Baudard, B.; Pasiliao, C.L. High strain-rate plastic deformation of molybdenum: Experimental investigation, constitutive modeling and validation using impact tests. *Int. J. Impact Eng.* **2016**, *96*, 116–128. [CrossRef]
30. Meyers, M.A. *Dynamic Behavior of Materials*; Wiley Interscience: Hoboken, NJ, USA, 1994.
31. Zhang, P.; Li, S.X.; Zhang, Z.F. General relationship between strength and hardness. *Mater. Sci. Eng. A* **2011**, *529*, 62–73. [CrossRef]
32. Steinberg, D.J. A rate-dependent constitutive model for molybdenum. *J. Appl. Phys.* **1993**, *74*, 3827–3831. [CrossRef]

Disclaimer/Publisher's Note: The statements, opinions and data contained in all publications are solely those of the individual author(s) and contributor(s) and not of MDPI and/or the editor(s). MDPI and/or the editor(s) disclaim responsibility for any injury to people or property resulting from any ideas, methods, instructions or products referred to in the content.